RSC Applied Interfaces

PAPER

View Article Online
View Journal | View Issue

Check for updates

Cite this: *RSC Appl. Interfaces*, 2025, **2**, 185

Supramolecular chemistry in solution and solid–gas interfaces: synthesis and photophysical properties of monocolor and bicolor fluorescent sensors for barium tagging in neutrinoless double beta decay†

Fernando Auria-Luna,[a] Frank W. Foss Jr.,[b] Juan Molina-Canteras,[a] Ivan Velazco-Cabral,[c] Aimar Marauri,[ad] Amaia Larumbe,[a] Borja Aparicio,‡[a] Juan Luis Vázquez,[c] Nerea Alberro,[a] Iosune Arrastia,[a] Virginia San Nacianceno,[a] Adai Colom,[ef] Carlos Marcuello,[d] Benjamin J. P. Jones,[b] David Nygren,[b] Juan J. Gómez-Cadenas,[eg] Celia Rogero,[gh] Iván Rivilla,*[eg] Fernando P. Cossío*[a] and the NEXT collaboration§

Received 21st June 2024,
Accepted 1st November 2024

DOI: 10.1039/d4lf00227j

rsc.li/RSCApplInter

Translation of photophysical properties of fluorescent sensors from solution to solid–gas environments *via* functionalized surfaces constitutes a challenge in chemistry. In this work, we report on the chemical synthesis, barium capture ability and photophysical properties of two families of monocolor and bicolor fluorescent sensors. These sensors were prepared to capture barium cations that can be produced in neutrinoless double beta decay of Xe-136. These sensors incorporate crown ether units, two different fluorophores, aliphatic spacers of different lengths, and a silatrane linker that forms covalent bonds with indium tin oxide (ITO) surfaces. Both species shared excellent Ba^{2+} binding abilities. Fluorescent monocolor indicators (FMIs), based on naphthyl fluorophores, showed an off–on character in solution controlled by photoinduced electron transfer. Fluorescent bicolor indicators (FBIs), based on benzo[*a*]imidazo[5,1,2-*cd*] fluorophores, exhibited a significant change in their emission spectra on going from the free to the barium-bound state. Both FMIs and FBIs showed similar photophysics in solution and on ITO. However, their performance on ITO was found to be attenuated, but not fully extinguished, with respect to the values obtained in solution, both in terms of intensity and selectivity between the free and Ba^{2+}-bound states. Despite this issue, improved performance of the FBIs based on confocal microscopy of the directly attached molecules was observed. These selective FMI and FBI chemosensors installed on tailor-made functionalized surfaces are promising tools to capture the barium cations produced in the double beta decay of Xe-136. The identification of this capture would boost the sensitivity of the experiments searching for the Xe-136-based neutrinoless double beta decay, as backgrounds would be almost totally suppressed.

Introduction

Double beta decay nuclear reactions[1] take place in certain privileged nuclides and result in the formation of daughter nuclides that are located two positions ahead along the periodic table of elements. In the Standard Model of particle physics, two neutrons of the parent nuclide are converted into two protons, with concomitant ejection of two electrons (beta

[a] Departamento de Química Orgánica I and Centro de Innovación y Química Avanzada (ORFEO-CINQA), Facultad de Química/Kimika Fakultatea, Universidad del País Vasco/Euskal Herriko Unibertsitatea (UPV/EHU), 20018 Donostia-San Sebastián, Spain. E-mail: fp.cossio@ehu.es
[b] Department of Chemistry and Biochemistry, University of Texas at Arlington, Arlington, Texas 76019, USA
[c] Department of Chemistry, University of Guanajuato, 36050 Guanajuato, Gto, Mexico
[d] Biofisika Institute (CSIC, UPV/EHU), 48940 Leioa, Spain
[e] Ikerbasque, Basque Foundation for Science, 48009 Bilbao, Spain
[f] Department of Biochemistry and Molecular Biology, Faculty of Science and Technology, Campus Universitario, Universidad del País Vasco/Euskal Herriko Unibertsitatea (UPV/EHU), 48940 Leioa, Spain
[g] Donostia International Physics Center (DIPC), 20018 Donostia-San Sebastián, Spain. E-mail: ivan.rivilla@ehu.es
[h] Materials Physics Center (CSIC-UPV/EHU), San Sebastián, E-20018, Spain

† Electronic supplementary information (ESI) available. See DOI: **https://doi.org/10.1039/d4lf00227j**

‡ Present address: Centro de Investigación en Química Biolóxica e Materiais Moleculares (CiQUS) and Departamento de Química Orgánica, Universidade de Santiago de Compostela, 15782 Santiago de Compostela, Spain.

§ The full NEXT collaboration author list is indicated in the ESI.

particles) and two antineutrinos, as shown in eqn (1). This process is denoted as the two neutrino double beta decay reaction ($\beta\beta2\nu$):

$$ {}^{N}_{Z}X \xrightarrow{\beta\beta2\nu} {}^{N}_{Z+2}Y^{2+} + 2e^{-} + 2\bar{\nu}_{e} \quad (1) $$

This nuclear reaction is an extremely rare event which has been observed in a number of nuclei with typical half-lives in the range of $>10^{26}$ years (ref. 2 and 3) (for comparison, the age of the universe is estimated to be 13.8×10^{9} years).[4] Another hypothetical process beyond the Standard Model is the neutrinoless double beta decay ($\beta\beta0\nu$), in which no neutrinos are emitted, thus releasing the daughter nuclide and two electrons of higher energy, as gathered in eqn (2):

$$ {}^{N}_{Z}X \xrightarrow{\beta\beta0\nu} {}^{N}_{Z+2}Y^{2+} + 2e^{-} \quad (2) $$

This latter reaction implies that neutrinos are Majorana particles,[5] namely they are their own antiparticles ($\nu_e = \bar{\nu}_e$). Experimental verification of this hypothesis would have profound consequences in particle physics and cosmology, by providing a key element for leptogenesis and the baryon asymmetry in the universe.[6,7]

One isotope that can experience double beta decay reactions is Xe-136 (${}^{N}_{Z}X = {}^{136}_{54}\mathrm{Xe}$), whose $\beta\beta x\nu$ (x = 0, 2) reaction leads to a Ba-136 dication[8](${}^{N}_{Z+2}Y^{2+} = {}^{136}_{56}\mathrm{Ba}^{2+}$). The current best lower limit to the half-life of this process is 2.3 × 10^{26} years (90% C.L.).[3] In the context of the future generation of Xe-based $\beta\beta0\nu$ $\left({}^{136}_{54}\mathrm{Xe} \xrightarrow{\beta\beta0\nu} {}^{136}_{56}\mathrm{Ba}^{2+} + 2e^{-}\right)$ experiments, the detection of the barium dication and its correlation with the experimental signal of the two electrons (so-called barium tagging) would lead to a virtually background-free experiment.

The general concept was proposed by Nygren[9] in 2015, and since then, several proofs of concept have been reported.[10,11] In the conceptual device named BOLD (Barium atOm Light Detector, see Fig. 1a), a xenon time-projection chamber (Xe-TPC) splits the products of the $\beta\beta0\nu$ reaction by drifting the electrons[12] towards the energy-tracking detector (ETC) and measures the energy of the event in order to distinguish between $\beta\beta0\nu$ and $\beta\beta2\nu$ disintegrations. The barium cation, whose drift can be estimated from the ETC data, goes towards the barium target detector (BTD). The best option for a BTD consists of a conducting surface anchored to a fluorescent sensor, which changes its properties once bounded to the barium cation.[9,11] A suitable optical detector (Fig. 1a) reads the fluorescent signal emitted by the bounded species after laser excitation at the adequate wavelength.[13] The fluorescent sensor incorporates a linker, a spacer covalently bonded to the fluorophore and a barium catcher (Fig. 1b). Given the extremely low production rate of $\beta\beta0\nu$ events (*vide supra*), the following requirements must be fulfilled by any fluorescent sensor incorporated to the BTD:

(i) The binding constant must be sufficiently high in order to ensure any Ba^{2+} species are captured;

(ii) The binding moiety must capture Ba^{2+} with high selectivity with respect to other species present in the Xe-TPC; and

(iii) The background must be extremely low in order to yield a suitable signal-to-noise ratio.

Although the photophysics of the supramolecular chemistry of cation capture is well known, its translation to solid–gas interfaces, in particular to a high-pressure xenon chamber (HPXe), is far from being well understood. The non-fluorescent surface must be passivated, such that competitive binding is unlikely and/or highly reversible. Within this context, in this work, we report on the chemical synthesis, barium capture ability, and fluorescence properties of two conceptually different families of barium tagging sensors anchored to a conducting surface formed by indium tin oxide (ITO).

Results and discussion

Design

We decided to incorporate silatranes as partially *N*-protected linkers[14] in the two families of fluorescent sensors because of their synthetic accessibility and the effective binding reaction of this species to metallic oxides such as ITO to yield covalently bound siloxane species (Fig. 2).[15] Aliphatic chains of two different lengths were selected in order to minimize the number of heteroatoms possessing lone pairs that could compete with the Ba^{2+} catcher during the cation-binding process. Aza-crown ethers[16,17] were chosen for Ba^{2+} capture because of the well-known capability of these cyclic compounds to bind cations with high selectivity and because of the highly preorganised character of these cyclic structures, which minimizes the entropic penalty associated with Ba^{2+} binding. Two schemes were considered: depending upon the number of nitrogen atoms incorporated into the 18-crown moiety. We denoted these structures as NO_5 and N_2O_4, associated with 1,4,7,10,13-pentaoxa-16-azacyclooctadecane and 1,4,10,13-tetraoxa-7,16-diazacyclooctadecane, respectively. These patterns were selected in order to assess the effect of nitrogen atoms on the binding constant.

The nature of the fluorophore installed in the sensor determines the design of this essential component. One possibility consists of incorporating a fluorophore that is inactive in the absence of the cation, for instance by deactivation *via* photoinduced electron transfer (PET).[18]

According to this approach, cation binding induces coordination of the nitrogen lone pair of the aza-crown ether, thus inhibiting the PET deactivation. This situation results in an off–on scheme (Fig. 2a) in which the absorbed and emitted wavelength is the same, the intensity being the factor that governs the identification of the bound state. We denote this kind of sensor as a fluorescent monocolor indicator (FMI). This approach has been successfully explored by the NEXT collaboration[19,20] *via* the incorporation of fluorophores based on naphthalimides (1*H*-

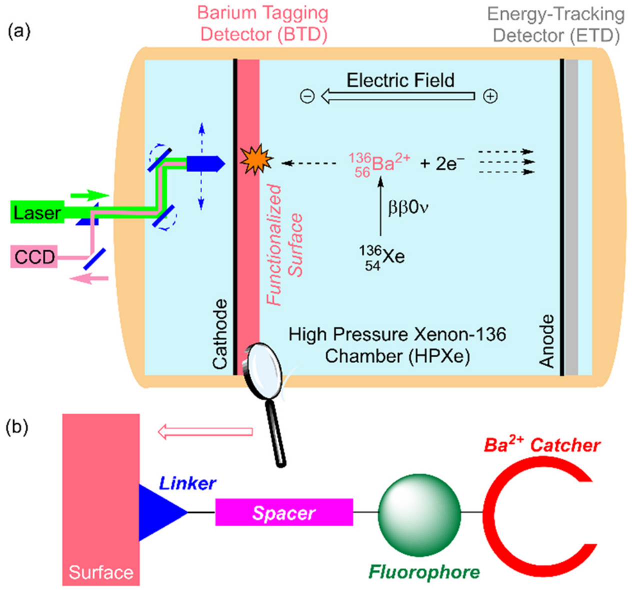

Fig. 1 (a) Basic design of a BOLD (Barium atOm Light Detector) device for the neutrinoless double beta decay ($\beta\beta0\nu$) of ^{136}Xe into $^{136}Ba^{2+}$. (b) Cartoon showing the components of a fluorescent indicator covalently anchored on an indium tin oxide (ITO) functionalized surface.

benzo[*de*]isoquinoline-1,3(2*H*)-diones). Another possibility consists of installing a two-component fluorophore whose photochemical spectrum depends on the coordination with Ba^{2+}. In the absence of cation binding, the two components participate in extended π-symmetric molecular orbitals, and the emission spectrum results in a well-defined signal. After Ba^{2+} capture, the proximal component of the fluorophore interacts with the cation, disrupting the coupling between both components and inducing a blue shift in the corresponding absorption and emission spectra (Fig. 2b). As a model fluorophore, we selected the 1-arylbenzo[*a*]imidazo[5,1,2-*cd*]indolizine scaffold.[21] We denoted this kind of fluorophore as a fluorescent bicolor indicator (FBI). This approach has also been successfully explored by the NEXT collaboration both in solution and in solid–gas interfaces involving chemisorbed species.[22,23]

In view of these encouraging precedents, we decided to synthesize novel fluorescent ionophore molecules incorporating Ba^{2+} catchers of type NO_5 and N_2O_4, FMI and FBI fluorophores, aliphatic spacers, and a silatrane unit as a linker to be incorporated on the ITO surface. The details about the chemical synthesis of these compounds are described and discussed in the next section.

Chemical synthesis

The synthesis of 1,8-naphthalimide FMI sensors was based on the method previously reported by Thapa *et al.*[20] Nucleophilic substitution reaction between mono- and diaza-crown ethers **1a,b** and 1-fluoro–4-nitrobenzene resulted in

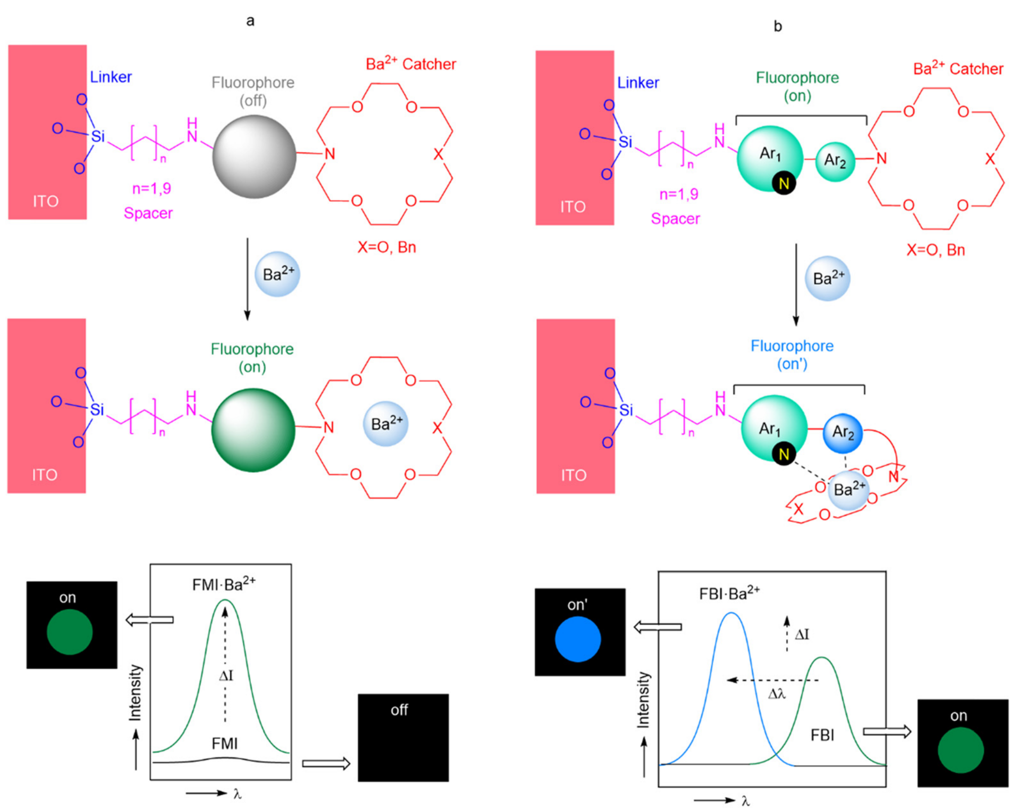

Fig. 2 Fluorescent monocolor indicators (FMIs, a) and fluorescent bicolor indicators (FBIs, b) anchored to an indium tin oxide surface, as analyzed in the present work. The changes in intensity and/or wavelength in the emission spectra are highlighted.

the formation of compounds **2a** (ref. 24) and **2b**, whose catalytic hydrogenation in a flow reactor was followed by expeditious condensation with 1,8-naphthalanhydride **3** yielded imides **4a,b**.[20] Fortunately, once the imides were obtained, they were found to be stable from degradation induced by water or air. After this step, diaza-crown ether **4b** was transformed into its *N*-benzyl derivative **4c** in acceptable yield. In a parallel sequence, triethoxy(ω-aminoalkyl)silanes **5a,b** were transformed into the corresponding silatrane derivatives **6a,b** in excellent yields. Coupling between these latter linker-spacer components with the complementary fluorophore-aza-crown counterparts **4a** and **4c** led to the desired FMI compounds **7aa–7bb**. Interestingly, N_2O_4 FMIs **7ba** and **7bb** were obtained in higher yields with respect to their NO_5 analogs, **7aa** and **7ab**. In all cases, the purity and scalability of this convergent synthesis were adequate for further analysis (Scheme 1).

The convergent synthesis of FBI molecules (Scheme 2) started with the formation of *N*-phenyl aza-crown ethers **8a** (ref. 25) and **8b**. Reaction with *N*-iodosuccinimide (NIS) of these latter compounds yielded the corresponding *para*-iodo derivatives **9a,b**. *N*-Benzylation of **9b** yielded **9c** with acceptable yield. C–B coupling between **9a,c** and bis(pinacolato)diboron (pinB–Bpin) resulted in the formation of the corresponding pinacolyl boronates **10a,b**. The synthesis of the 1-arylbenzo[*a*]imidazo[5,1,2-*cd*]indolizine scaffold fluorophore started with a double condensation of amino ester **11** with methyl bromoacetate, followed by a reaction with phosphoryl chloride.[26] Chloride derivative **12a** was transformed into its iodo congener **12b**, and then, a formal (8 + 2) thermal cycloaddition[27] with benzyne formed *in situ* from 2-(trimethylsilyl)phenyl triflate yielded the tetracyclic methyl ester **13**. Suzuki[28]–Miyaura[29] reaction of this latter higher order cycloadducts with aryl aza-crown ether boronates **10a,b** led to the formation of compounds **14a,b**. Hydrolysis of the ester moiety followed by amide coupling with ω-aminoalkyl silatranes **6a,b** yielded the final FBI compounds **15aa–bb**. In summary, our convergent syntheses of FMI and FBI sensors took place with moderate to low overall yields but with high purity, which was useful for further purposes in this work.

In order to prepare functionalized surfaces on ITO (or quartz, if desired), after intensive exploration of different experimental conditions, we optimized the procedure indicated in the following lines. First, indium tin oxide was pre-activated by O_2 plasma for 90 min (Fig. 3, step a) and kept under vacuum at 60 °C for 1–3 h in the pre-chamber of the glove box (Fig. 3, step b). Meanwhile, 0.46 mM solutions of compounds **7aa–bb** or **15aa–bb** in MeCN were prepared in the glove box. The activated surface was introduced in the glove box and put in the spin coater. Then, a previously prepared solution containing compound **7** or **15** (3 μL) was deposited on the pre-activated surface and spin-coated under reduced pressure for 10 s at 1000 rpm (spin-up/spin-off and curing). This process was followed 3 times (Fig. 3, step c). The sample thus obtained was taken out from the glove box and washed with 10 mL of MeCN (Fig. 3, step d), kept for 10 min with 10 mL of MeCN in the ultrasonic bath (Fig. 3, step e), washed again with 10 mL of MeCN (Fig. 3, step f), and dried with Ar flux (Fig. 3, step g). For the reaction with barium, the functionalized surface was put again in the spin coater. Then, 10 μL of a saturated solution of $Ba(ClO_4)_2$ in MeCN were added dropwise and the resulting mixture was spin-coated under reduced pressure for 20 s at 1200 rpm. The subsequent

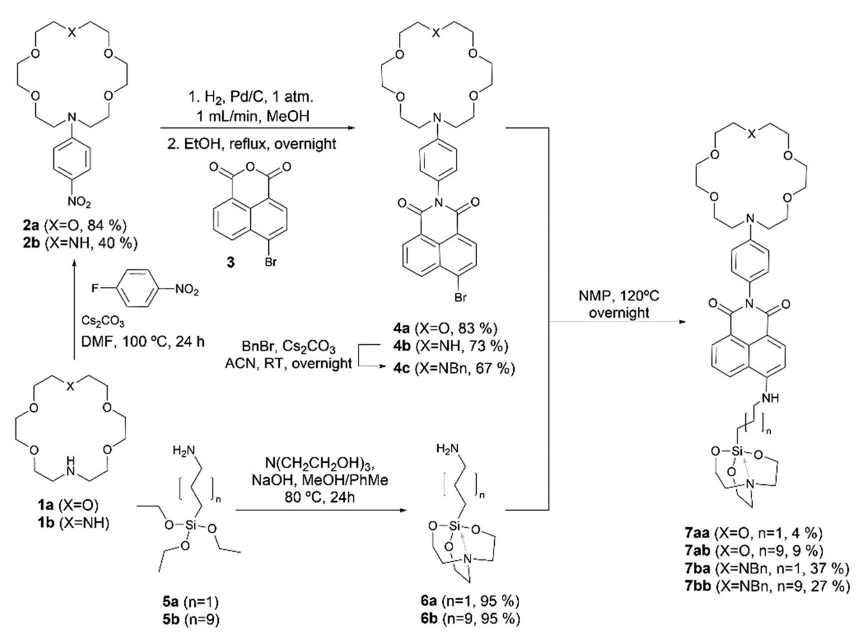

Scheme 1 Synthesis of fluorescent monocolor indicators (FMIs) **7aa–bb** from crown ethers **1a,b**, naphthyl fluorophore **3** and silatranes **6a,b**. NMP: *N*-methylpyrrolidone; ACN: acetonitrile; RT: room temperature.

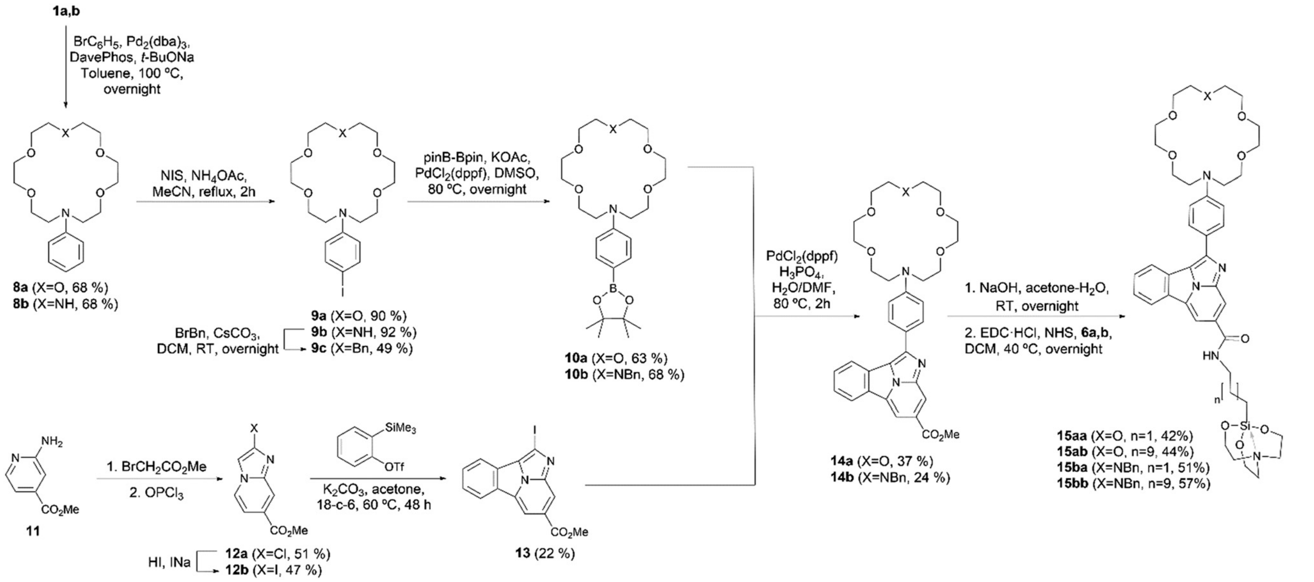

Scheme 2 Synthesis of bicolor fluorescent indicators **15aa–bb** from crown ethers **1a,b**, benzo[*a*]imidazo[5,1,2-*cd*]indolinizin-1-yl fluorophore **13** and silatranes **6a,b**. ACN: acetonitrile; DCM: dichloromethane; RT: room temperature; EDC·HCl: *N*-(3-dimethylaminopropyl)-*N*′-ethylcarbodiimide hydrochloride; NHS: *N*-hydroxysuccinimide.

treatment was that described for the previous d–g steps. This procedure was carried out in order to generate functionalized surfaces in which sensors **7** and **15** were covalently linked to ITO or quartz. These experiments were carried out in quintuplicate. Washing, sonication and drying steps (denoted as c–g in Fig. 3) were conducted to eliminate the triethanolamine equivalent stemming from the silatrane moiety, as well as any unreacted FMI or FBI molecule, as shown in Scheme 3. In a subsequent step, addition of a solution of $Ba(ClO_4)_2$ on this functionalized surface, followed by the corresponding washing and drying steps, resulted in the functionalized surfaces containing the Ba^{2+}-coordinated form of FMIs **7** and FBIs **3** represented in Scheme 3.

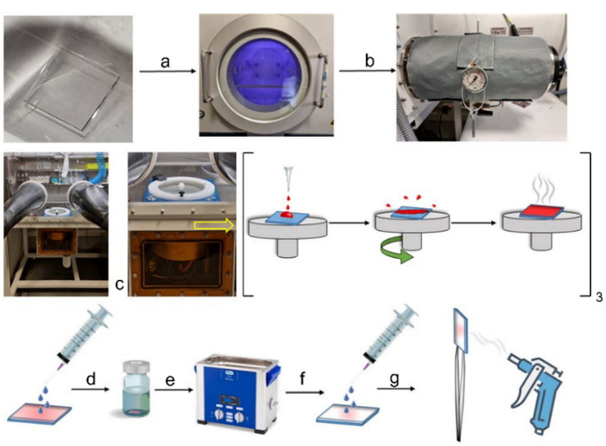

Fig. 3 Protocol for the preparation of functionalized monolayers incorporating the fluorescent sensor on ITO. (a) O_2-activated plasma; (b) vacuum at 60 °C; (c) spin coating; (d) washing; (e) sonication; (f) washing; and (g) drying.

Alternatively, barium was deposited by sublimation of $Ba(OTf)_2$ because of the lower melting point of this latter salt with respect to $Ba(ClO_4)_2$ (see ESI,† section 2, page S3).

In order to determine the average height of our sensor layer deposited on ITO, an AFM scratch experiment was performed on the surface using the cantilever itself (Fig. 4). Scratching experiments conducted on metallic glasses,[30] metal thin films,[31] and soft polymer systems[32] can be found in the literature. In our case, as an example, AFM scratching experiments for **15ba** were carried out (Fig. 4). These experiments (Fig. 4, panel e) revealed a height difference of 2.11 nm between ITO (Fig. 4, panels a and c) and ITO covalently bound to **15ba** (Fig. 4, panels b and d). This experimental height average value was found to be in good agreement with the theoretically calculated value of 2.14 nm (Fig. 4, panel f). According to our calculations, the folded conformation of **15ba** is due to the π-stacking between the fluorophore and the *N*-benzyl group of the diaza-crown ether moiety.

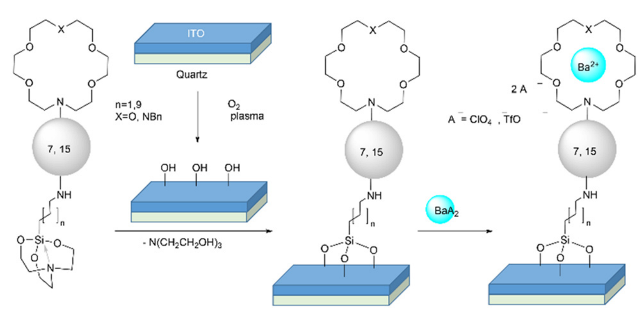

Scheme 3 Chemical transformations leading to ITO-based functionalized surfaces containing free and Ba^{2+}-bound sensors **7** (FMIs) and **15** (FBIs), respectively.

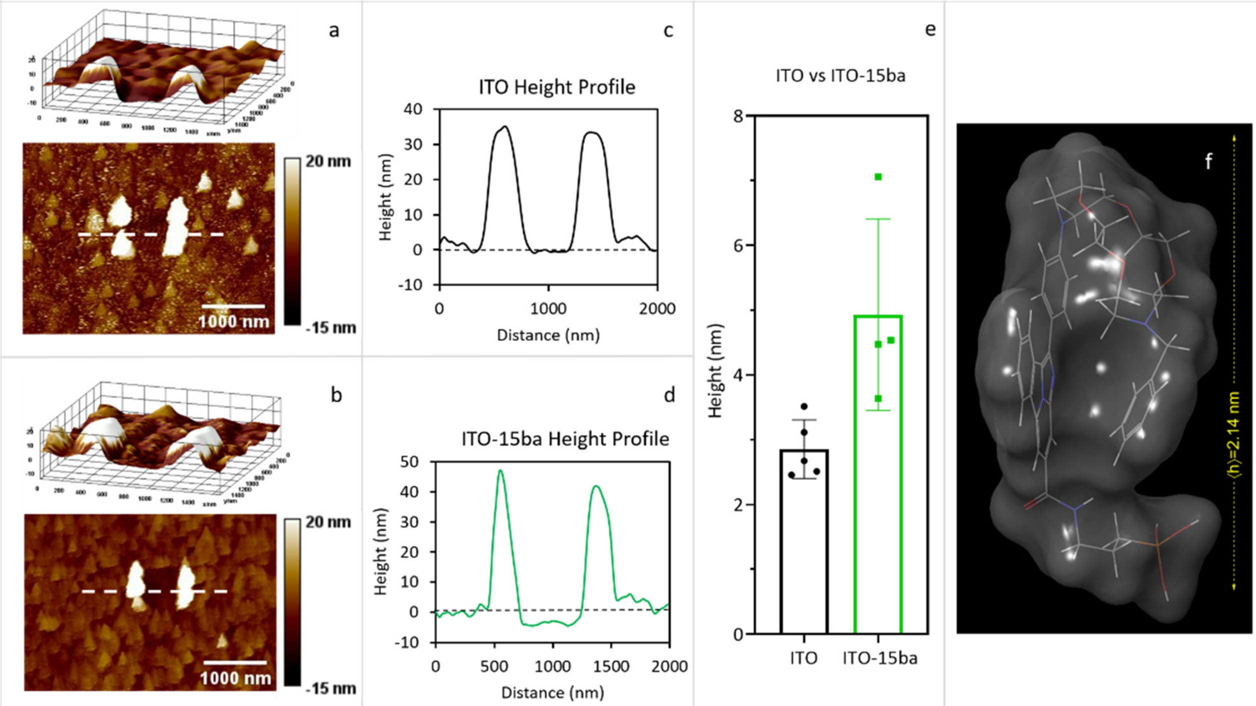

Fig. 4 a) Representative 3D and 2D topography images of a scratched ITO surface area. b) Representative 3D and 2D topography images of a scratched ITO-**15ba** surface area. c) Cross section of image a. d) Cross section of image b. e) Box plot of the statistical analysis of the difference of height found in the scratched ITO (black colour) and ITO-**15ba** (green colour) sample surfaces. e) Theoretical height of a **15ba** molecule calculated by MM3 molecular dynamics followed by RHF/PM6 optimization.

Barium capture and photophysical properties

We started the photophysical measurements by determining the emission wavelengths (λ_{em}) at the most efficient excitation wavelengths (λ_{exc}), which was previously determined for each sensor (see ESI† section 5 pag. S93). All the Job's plots showed that each FMI and FBI molecule captured one and only one barium cation. The different

Table 1 Emission wavelengths (λ_{em}), differences in wavelengths between the Ba^{2+}-bound and free states ($\Delta\lambda$), molecular discrimination factors (f_λ), quantum yields (ϕ_λ) and molar extinction coefficients (ε_λ) of compounds **7aa–bb**, **14a,b** and **15aa–bb**

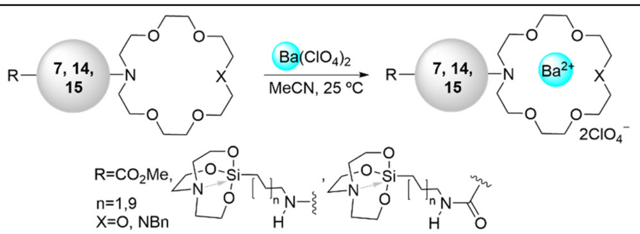

Sensor	λ_{em}[a] [nm] Free	λ_{em}[a] [nm] Ba^{2+}	$\Delta\lambda$[b] [nm]	f_λ[c]	ϕ_λ Free	ϕ_λ Ba^{2+}	ε_λ [M^{-1} cm^1] Free	ε_λ [M^{-1} cm^1] Ba^{2+}
7aa	534	538	−4	34	0.01	0.62	2169	9737
7ab	528	532	−4	4	0.11	0.57	5408	5359
7ba	536	540	−4	64	0.01	0.92	7618	9016
7bb	528	534	−6	71	0.01	0.89	13 444	13 568
14a	520	431	89	61	0.89	0.51	12 971	7244
14b	514	432	82	8	0.68	0.38	9259	14 910
15aa	508	434	74	285	0.93	0.35	10 226	5572
15ab	504	432	72	66	0.79	0.33	10 165	4889
15ba	502	432	70	89	0.92	0.94	27 031	10 196
15bb	505	432	73	134	0.93	0.62	6875	6867

[a] Values measured after excitation at the optimal wavelength. [b] Computed by means of eqn (3). [c] Computed according to eqn (4), measured at the max. emission wavelength of the chelated species.

values are collected in Table 1. Then, we compared these values for each free compound with the corresponding values upon Ba^{2+} capture, according to the following expression:

$$\Delta\lambda = \lambda_{em}(\text{free}) - \lambda_{em}(Ba^{2+}) \tag{3}$$

According to the data gathered in Table 1, for compounds **7** $\Delta\lambda \approx 0$, thus confirming the monocolor character of these FMI sensors. In contrast, for the FBI family of sensors, the $\Delta\lambda$ values ranged from 70 to 89 nm. We also calculated for each molecule the dimensionless peak discrimination factor[23] f_λ at a given wavelength λ, defined as indicated in eqn (4):

$$f_\lambda = \frac{I_\lambda(Ba^{2+}) - I_\lambda(\text{free})}{I_\lambda(\text{free})} \tag{4}$$

where $I_\lambda(Ba^{2+})$ and $I_\lambda(\text{free})$ are the intensities of the emission signals at the wavelength of the corresponding bound and free fluorophore, respectively. Our results indicate that the f_λ values can vary from 4 to 285 (see Table 1). However, the reasons for these different values are different. In the case of FMIs **7aa–bb**, the magnitude depends only on the intensity values since $\Delta\lambda \approx 0$. In contrast, the situation in FBIs **14a,b** and **15aa–bb** depends on the intensities of the emission signals with different λ_{em} values at the free and bound states. These different situations are exemplified in Fig. 5. Compounds **15aa** and **15bb** show the highest f_λ values, thus suggesting their promising character as NEXT sensors.

The quantum yields ϕ_λ reveal the deep differences between both types of sensors. In the case of FMIs **7aa–bb**, the ϕ_λ values are very low in the absence of barium, whereas these quantum yields are much higher when these molecules are bound to Ba^{2+}. Thus, incorporation of the spacer and linker units in these FMI sensors does not modify significantly their photophysical properties in solution.[33] In the case of FBI molecules **14a,b** and **15aa–bb** the values are higher when Ba^{2+} is not present. The differences in the molar extinction coefficients at the free and Ba^{2+}-bound states are lower in comparison. However, with the exception of **15bb**, FBI compounds **15** show higher values in the absence of the barium cation. The absorption cross sections (in Å^2), computed according to eqn (5), follow the same trends (see Table 2).

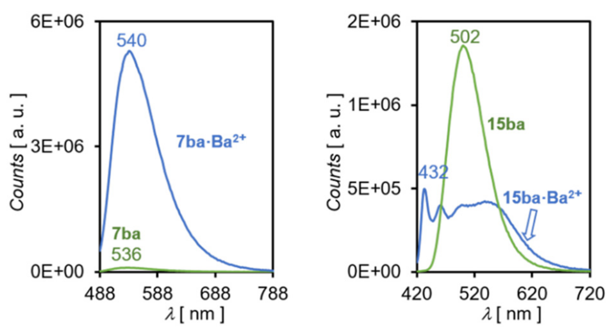

Fig. 5 Emission spectra in acetonitrile solution of FMI sensor **7ba** and FBI sensor **15ba** at their respective free and barium-bound states.

$$\sigma_\lambda = \frac{\ln(10) \times 10^{19}}{N_A}\varepsilon_\lambda \tag{5}$$

Because of these latter features, the molecular brightness[34] B_λ, defined as

$$B_\lambda = \phi_\lambda \cdot \varepsilon_\lambda \tag{6}$$

results in distinct behavior for FMI and FBI compounds, as shown in Table 2. In effect, monocolor sensors **7** show much higher brightness when bound to Ba^{2+}, whereas bicolor compounds **14** and **15** show comparable brightness at both states, the values associated with the respective unbound states being in general one order of magnitude higher. From these results, we conclude that it would be desirable that in future developments, the FBI sensors possess higher quantum yields in the Ba^{2+}-bound state.

Binding constants[35] associated with the scheme shown in Table 1 were obtained according to the following equation:

$$\frac{[Ba^{2+}]}{\varepsilon_{\text{free}} - \varepsilon_{\text{app}}} = \frac{[Ba^{2+}]}{\varepsilon_{\text{free}} - \varepsilon_{\text{bound}}} + \frac{1}{K_b(\varepsilon_{\text{free}} - \varepsilon_{\text{bound}})} \tag{7}$$

where K_b is the binding constant, $\varepsilon_{\text{free}}$ is the extinction coefficient of the free sensor, ε_{app} represents the apparent extinction coefficient, calculated as the ratio between the observed absorbance and the concentration of the sensor in each experiment, and $\varepsilon_{\text{bound}}$ stands for the extinction coefficient of the complex bound to Ba^{2+}. Plotting $[Ba^{2+}](\varepsilon_{\text{free}} - \varepsilon_{\text{app}})$ *vs.* $[Ba^{2+}]$ for each experiment and performing a linear fitting gives an equation $y = mx + n$, in which the binding constant corresponds to $K_b = m/n$ (see ESI† Fig. S3). From the values obtained for K_b (see Table 2), we concluded that the effect of the additional nitrogen atom is not always associated with a higher binding constant. Thus, in the case of the FMI series, the highest value is obtained for **7ba** possessing a N_2O_4 binding unit, which corresponds to the biggest binding constant. In contrast, the highest value for the FBI series is found for **15ab**, which includes a NO_5 mono aza-crown ether as a Ba^{2+} catcher moiety. In any case, the K_b values reported in

Table 2 Molecular brightness parameters (B_λ), absorption cross sections (σ_λ) and binding constants (K_b) of compounds **7aa–bb**, **14a,b** and **15aa–bb**

	B_λ[a] [M^{-1} cm^{-1}]		σ_λ[b] [Å^2]		
Sensor	Free	Ba^{2+}	Free	Ba^{2+}	K_b[c] [M^{-1}]
7aa	23	6037	0.08	0.37	4.34×10^4
7ab	595	3055	0.21	0.20	3.16×10^5
7ba	76	8295	0.29	0.34	1.92×10^6
7bb	13	12 076	0.51	0.52	7.21×10^4
14a	11 544	3694	0.50	0.28	4.13×10^5
14b	6296	5666	0.35	0.57	5.44×10^5
15aa	9510	1950	0.66	0.21	1.95×10^5
15ab	8030	1613	0.39	0.19	5.25×10^5
15ba	24 869	9584	1.03	0.39	1.79×10^5
15bb	6394	4257	0.26	0.26	1.77×10^5

[a] Computed by means of eqn (6). [b] Computed by using eqn (5). [c] Calculated by means of eqn (7).

Table 2 are close enough to each other and high enough to warrant an efficient ion capture, essential for a future BOLD device. This result suggests that in future designs, the NO_5 or N_2O_4 nature of the crown ether will not be a critical factor and both cyclic ether systems must be considered since the structure–activity relationship of both macrocyclic barium catchers is not readily predictable.

In general, selectivity is an essential feature of a sensor aiming to bind a given cation. In the NEXT experiment, since only Ba^{2+} is generated *via* $\beta\beta n\nu$ (n = 0, 2) within the Xe-TPC, no competitive sensor–cation interactions are expected. However, the interaction of all the molecules reported in Table 2 with other cations was studied in order to consider the potential utility of these sensors in future developments, especially in biological systems. Single cations such as Na^+ and K^+ and several dications from the alkaline earth group were selected for these experiments (see ESI† section 5). In the case of the monocolor series **7**, Ba^{2+} and Sr^{2+} produce an enhancement in emission intensity, while Ca^{2+} does so to a lesser extent. On the other hand, in the bicolor series **14** and **15**, Ba^{2+} and Sr^{2+} produce FBI signals, with high hypsochromism, while Mg^{2+} generates a decrease in intensity. Na^+ and K^+ do not produce significant changes with respect to the unbound state. The behavior of both NO_5 and N_2O_4 crown ether moieties was indistinguishable. As a general trend, Sr^{2+} and Ba^{2+} trigger the same good response in all cases, while Ca^{2+} and Mg^{2+} seem to partially bind to FMIs and FBIs, respectively. The rest of the tests did not produce appreciable changes in the emission spectra, showing a trend in which bigger cations produce more substantial effects related to a better binding to the sensor, as reported in previous studies.[19,22]

The limits of detection (LODs) for all the compounds reported in Table 2 were also calculated, obtaining values ranging from 0.059 to 0.351 μM and from 0.127 to 0.392 μM for the FMI and FBI families, respectively (see ESI† Table S1). These values are comparable to other fluorimetric sensors for Ba^{2+} reported in the literature.[36–40]

In order to get a better understanding of the low intensity of photoemission of naphthyl *N*-phenyl imide fluorophores **7aa–bb**, we performed complete active space self-consistent field (CASSCF) calculations on model compound **16** (Fig. 6) as a preliminary step. These calculations involved four electrons distributed in three canonical molecular orbitals (MOs), denoted as CASSCF(4,3). Our results show a non-coplanar arrangement of the *para*-phenylene group with respect to the naphthylimide moiety induced by the steric repulsion between the oxygen atoms and the *ortho* hydrogens of the phenylene group, with a dihedral angle of *ca.* 90 deg (Fig. 6). This nonplanar arrangement in turn generates a decoupling between the π-MOs of both components. The adiabatic $S_0 \rightarrow S_1^*$ excitation occurs between HOMO−1 and LUMO. From this configuration, the system relaxes to the S_1 state *via* a PET from HOMO to HOMO−1 (Table 3). From this latter state, the $S_1 \rightarrow S_0$ transition is less efficient, thus resulting in the *off* state of this class of chromophores **7** in the absence of Ba^{2+}.

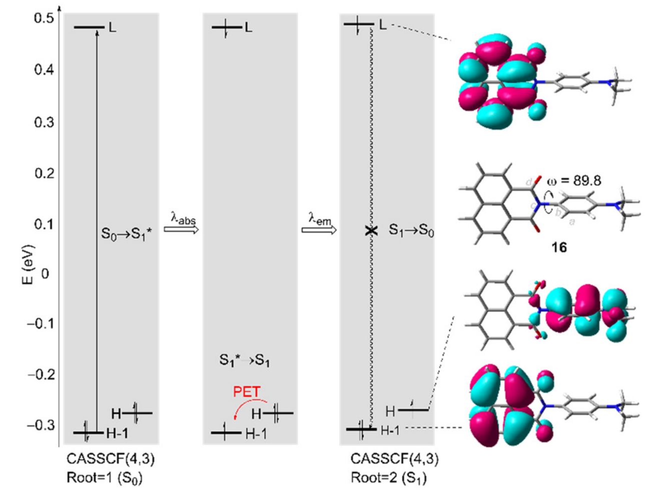

Fig. 6 Single-point CASSCF(4,3)/6-31G*//HF/6-31G* calculations of 2-(4-(dimethylamino)phenyl)-1*H*-benzo[*de*]isoquinoline-1,3(2*H*)-dione **16**. H and L stand for HOMO and LUMO, respectively. The photoinduced electron transfer (PET) in the relaxed first single state (S_1) is shown. Dihedral angle ω = (a, b, c, d) is given in deg.

The photophysical properties of FMI and FBI compounds were rationalized by means of time-dependent DFT (TD-DFT)[41] calculations.[42–44] The chief electronic features associated with the lowest $S_0 \rightarrow S_1$ energy transition of a model FMI candidate are gathered in Fig. 7. As a model compound we chose compound **7aa′**, in which the spacer and silatrane units of **7aa** have been replaced with a computationally less demanding methylamino group. The TD-DFT calculations show that the lowest energy transitions are very similar in the absence of barium and after interaction with barium perchlorate. In both cases, the starting HOMO−1 and HOMO Kohn–Sham (KS) MOs are located on the naphthyl fluorophore, the *para*-substituted phenylidene group being in a non-coplanar conformation because of the repulsion induced by the imide carboxy groups. The LUMO+2 MOs show a higher participation of the phenylidene group, which is particularly relevant in the barium-free species **7aa′**. In addition, one of the oxygen atoms of the imide moiety interacts with the barium cation in **7aa′·Ba(ClO₄)₂** and acquires a charge of +0.08 e, whereas in **7aa′**, this charge is −0.25 e. In summary, these combined interactions result in a calculated adiabatic λ_{abs} of 401 nm, in good agreement with the experimentally observed value of 436 nm. When Ba^{2+} is coordinated, the computed λ_{abs} value is 395 nm, comparable with the experimental adiabatic value of 440 nm. These results are in qualitative agreement with the FMI character of compounds **7**.

The photophysical behavior of FBI sensors can be understood on the basis of the strong geometrical distortion induced by the barium cation. Fig. 8 shows the electronic and geometric features of ester **14a** in its unbound state and coordinated to barium perchlorate. At the free state the benzo[*a*]imidazo[5,1,2-*cd*]indolizine fluorophore and the 1,4-phenylidene ring are almost coplanar to each other and

Table 3 Symbolic density matrices[a] of model molecule **16** at the S_1 and S_0 (in parentheses) states

	HOMO−1	HOMO	LUMO
HOMO−1	2.0 (1.94200)		
HOMO	0.131355×10^{-4} (-0.234616×10^{-9})	1.0 (2.0)	
LUMO	-0.124577×10^{-4} (-0.124577×10^{-5})$^{-}$	0.811215×10^{-7} (0.147730×10^{-9})	0.999958 (0.579985×10^{-1})

[a] Calculated at the CASSCF(4,3)/6-31G*//HF/6-31G* level of theory.

act as a combined fluorophore. The absorption associated with the lowest energy transition yields a calculated λ_{abs} value of 431 nm, in nice agreement with the wavelength absorption of 438 nm found experimentally. In contrast, coordination to barium yields a calculated λ_{abs} value of 373 nm, the corresponding experimental value being 421 nm. Fig. 8 shows that the lowest adiabatic transition in **14a·Ba^{2+}** corresponds to a lower energy and it is linked to a crown ether–Ba^{2+}–π–N interaction, associated with a strong conformational change, with a benzo[*a*]imidazo[5,1,2-*cd*]indolizine-*p*-phenyl dihedral angle of *ca.* 105 deg at the ground S_0 electronic state.

The geometries of the four computed **7aa′**, **7aa′·Ba(ClO$_4$)$_2$**, **14a** and **14a·Ba(ClO$_4$)$_2$** species at the S_1 state and their superposition with the respective S_0 levels can be found in Fig. 9. These calculations were performed assuming that each fluorescent indicator captures one and only one Ba^{2+}, as demonstrated experimentally by Job's plot diagrams (see ESI.† section 5). In the case of **7aa′**, the geometries at both S_0 and S_1 states are nearly identical. In particular, the dihedral angle ω between the *para*-phenylene moiety and the naphthylimide fluorophore is close to 90 deg. at both electronic states because of the repulsion between the oxygen atoms and the *ortho* hydrogens of the *para*-phenylene group, as we have discussed in the case of model compound **16** (Fig. 6). This results in a separation between the π-MOs of both units. Thus, in the case of **7aa′** the calculated emission wavelengths are *ca.* λ_{em} = 421 nm and 430 nm for the free and Ba^{2+}-bound compounds, which corresponds to a $\Delta\lambda$ value of 9 nm, compatible with the FMI behavior of compounds **7** (Table 1).

FBI ester **14a** shows an optimized S_1-geometry very similar to that computed at the S_0 state, with dihedral values close to planarity (Fig. 7). The calculated λ_{em} value of **14a** is 478 nm, in acceptable agreement with the experimentally found value of 520 nm. Coordination of **14a** to Ba^{2+} results in a larger conformational change in which the S_0 and S_1 geometries are less superposable than those optimized for **7aa′·Ba(ClO$_4$)$_2$** (Fig. 9). In particular, the value of the dihedral angle ω at the S_1 state is larger than in the ground state but is enough to generate an FBI behavior, with λ_{em} = 411 nm for **14a·Ba(ClO$_4$)$_2$**, also in nice agreement with the experimental value of 431 nm (Table 1). These emission values result in a blue shift of $\Delta\lambda$ = 67 nm (eqn (3)), the experimental value being 89 nm (see Table 1). It is noteworthy that the computed spectrum of **14a·Ba(ClO$_4$)$_2$** shows two bands (see ESI,† Fig. S4). The less energetic one corresponds to a transition involving four KS MOs, whereas there is another more intense band associated with a complex ensemble of nine transitions, whose major contributions correspond to emissions at 328 nm and 298 nm. This situation is observed

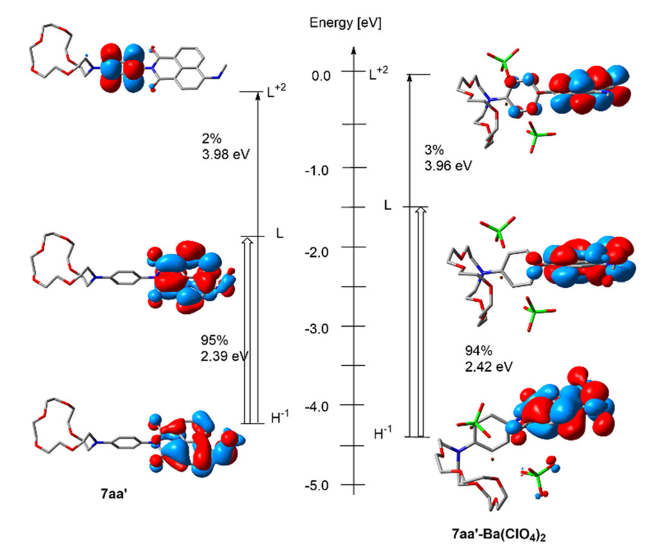

Fig. 7 Kohn Sham molecular orbitals and nature of the main transitions as determined by TD-DFT at the M06/6-311++G** (for **7aa′**) and M06/6-311++G**&Def2TZVPP (for **7aa′·Ba(ClO$_4$)$_2$**) levels of theory. H and L stand for HOMO and LUMO, respectively.

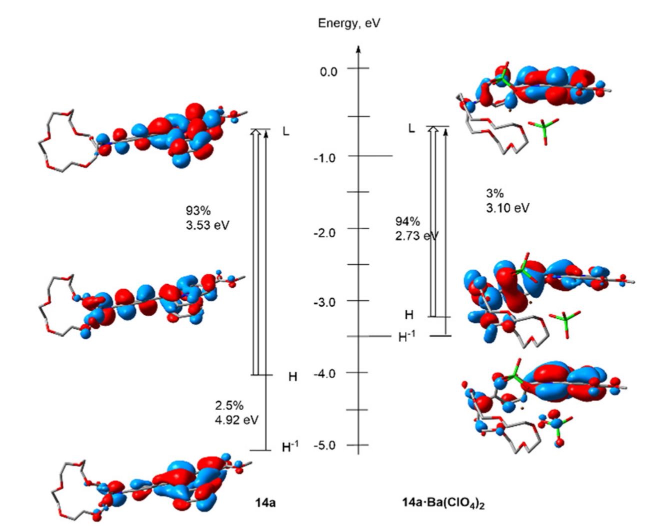

Fig. 8 Kohn Sham molecular orbitals and nature of the main transition as determined by TD-DFT at the M06/6-311++G** (for **14a**) and M06/6-311++G**&Def2TZVPP (for **14a·Ba(ClO$_4$)$_2$** levels of theory. H and L stand for HOMO and LUMO, respectively.

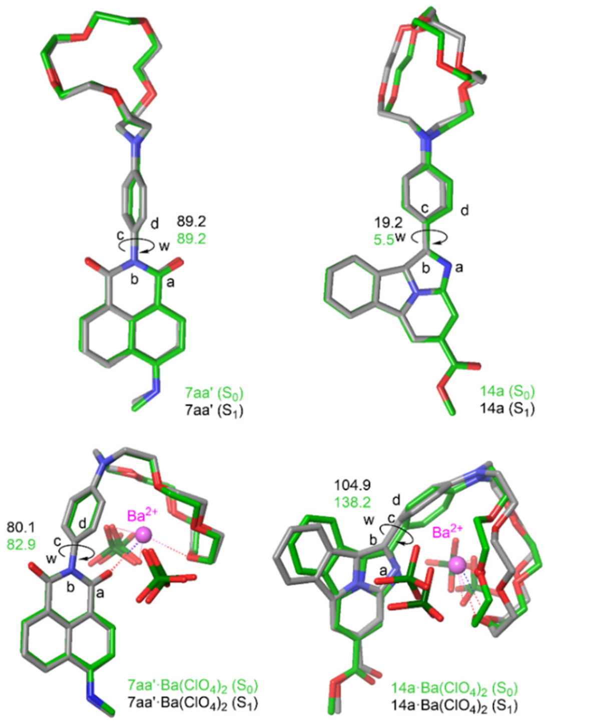

Fig. 9 Main geometric features of **7aa′**, **7aa′·Ba(ClO$_4$)$_2$**, **14a** and **14a·Ba(ClO$_4$)$_2$** species as optimized by TD-DFT at the S_1 state (carbon atoms in green). The geometries at the ground state S_0 level (in gray) are also shown for comparison.

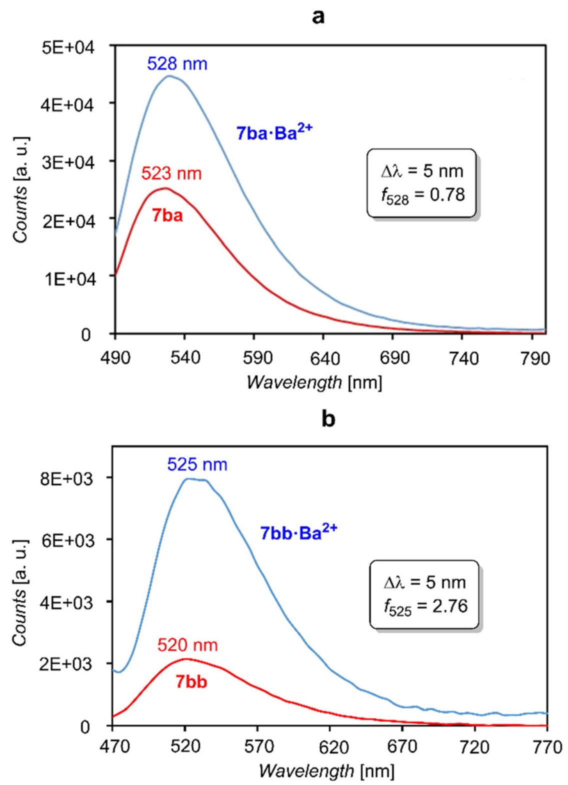

Fig. 10 (a) Emission spectra on ITO of free sensor **7ba** (red) and coordinated to Ba^{2+} (blue). (b) The same as (a) but with sensor **7bb**. The wavelength differences $\Delta\lambda_{em}$ and molecular discrimination factors f_λ are also given. The corresponding values obtained in solution are reported in Table 1.

in the experimental spectra recorded in solution. In the case of free FBI molecules, the larger conformational freedom of these species results in wider emission spectra with only one non-resolved band (see Fig. 11). In summary, these TD-DFT calculations provide a better understanding of the photochemical behavior of FMI and FBI sensors, which could be useful in further developments.

We next investigated the fluorescence of FMI and FBI sensors on functionalized surfaces. The results corresponding to the fluorescence spectra on ITO surfaces functionalized with species **7ba,bb** and their respective Ba^{2+} complexes are gathered in Fig. 10. It is interesting to indicate that in solid–gas interfaces the fluorescence spectra are significantly less intense, as it can be seen by comparison of the intensity numbers shown in Fig. 5 and 10. Actually, our attempts to explore these FMI compounds with confocal microscopy met with no success (see below). Most likely, another binding method such as dip coating of the acid derivatives instead of the silatranes used in our experiments should be used for these FMI sensors.[21,23] As expected, the emission wavelengths do not vary significantly on going from the free to the Ba^{2+}-bound species ($\Delta\lambda$ = 5 nm), thus confirming the FMI character of these sensors. However, our results indicate that the *off–on* character of both compounds effectively vanishes on ITO surfaces. In effect, the f_λ discrimination factors are much lower in both cases with respect to the values obtained in solution (see Table 1 and Fig. 10). A relatively bright state is observed in **7aa** and **7bb** in the absence of Ba^{2+}, while a reduced *on*-state is observed after Ba^{2+} addition by spin coating. Similar studies with FBI sensors showed that the intensities were also significantly lower than those measured in acetonitrile solution. This persistent partial quenching issue must be considered in further developments of FMI and FBI sensors. Actually, reduced fluorescence of dyes on ITO has been observed.[45]

Fig. 11 shows the behavior of FBI molecules **15aa** and **15ba**. The emission spectra measured in solution (Fig. 11, panels a and d) for the free species are more intense than those observed upon Ba^{2+} coordination. In addition, averaged spectra with only one wide signal were observed for FBI·Ba^{2+} complexes covalently anchored to ITO surfaces, most likely because of the average superposition of signals associated with different microenvironments around discrete species (Fig. 11). The corresponding $\Delta\lambda$ values are of *ca.* 70 nm. However, the molecular discrimination factor is significantly higher for **15aa** (f = 285) than for **15ba** (f = 89). When the same spectra were measured in the presence of $Ba(ClO_4)_2$ deposited on the ITO-FBI functionalized surface *via* spin coating, the $\Delta\lambda$ values measured for **15aa** and **15ba** were 107 and 92 nm, respectively. However, the molecular discrimination factors are much lower when measured on ITO. Thus, for **15aa** f_{420} = 10, and in the case of **15ba** a very low value of f_{422} = 1 was measured (Fig. 11, panel b and e),

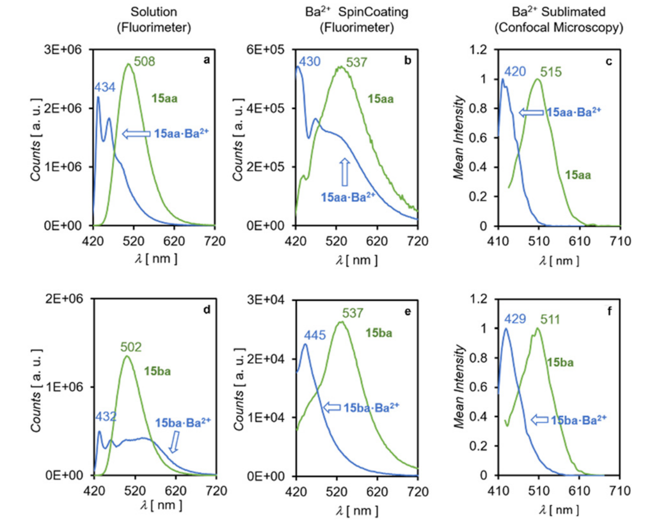

Fig. 11 Emission spectra observed for FBI molecules **15aa** (panels a–c) and **15ba** (panels d–f). The values obtained in solution are shown in panels a and d. Values corresponding to spin coating on ITO at the free state or in the presence of $Ba(ClO_4)_2$ are shown in panels b and e. Average emission spectra of a 24 × 24 μm surface, obtained through confocal microscopy (see ESI† section 2 pag. S2), collected for the free state and after sublimation of $Ba(TfO)_2$, are presented in panels c and f.

thus verging this molecule into the territory of FMI molecules. The main reason for this decrease is that there is a significant emission of the unbound states at the λ_{em} value of the chelated species.

A similar behavior was observed in confocal microscopy on samples of ITO with anchored **15aa** and **15ba** units upon sublimation with $Ba(OTf)_2$. Under these conditions, the measured $\Delta\lambda$ values for **15aa** and **15ba** were 95 nm and 82 nm, respectively (Fig. 11, panels c and f). These results correspond to the average of the scanned surfaces (see ESI† section 2 pag. S2) and are in line with those obtained by means of spin coating and show that emission spectra on anisotropic solid–gas interfaces are less selective than in solution. Unfortunately, FBI molecules **15ab** and **15bb** could not be measured because of their poor binding to the surfaces as well as their negligible fluorescence intensity, most likely because of disordered non-covalent stacking of the large aliphatic spacer–fluorophore moieties on the ITO surface. Similarly, FMI molecules **7aa–bb** could not be analysed by confocal microscopy because of their very low intensities observed under all tested conditions.

In contrast, a clear bicolor behavior of **15aa** and **15ba** was observed by confocal microscopy at selected wavelengths, as shown in Fig. 12, in which the emission signals of both FBIs in the free and Ba^{2+}-bound states are shown. In two separate series of experiments with **15aa** and **15ba**, identical samples containing each sensor were analysed after sublimation of barium triflate under conditions that permitted the coexistence of free and bound species. Excitation of both sensors at 405 nm resulted in clear emission signals within the 480–700 nm range (green color), associated with spots indicating the absence of barium (Fig. 12, panels a and d).

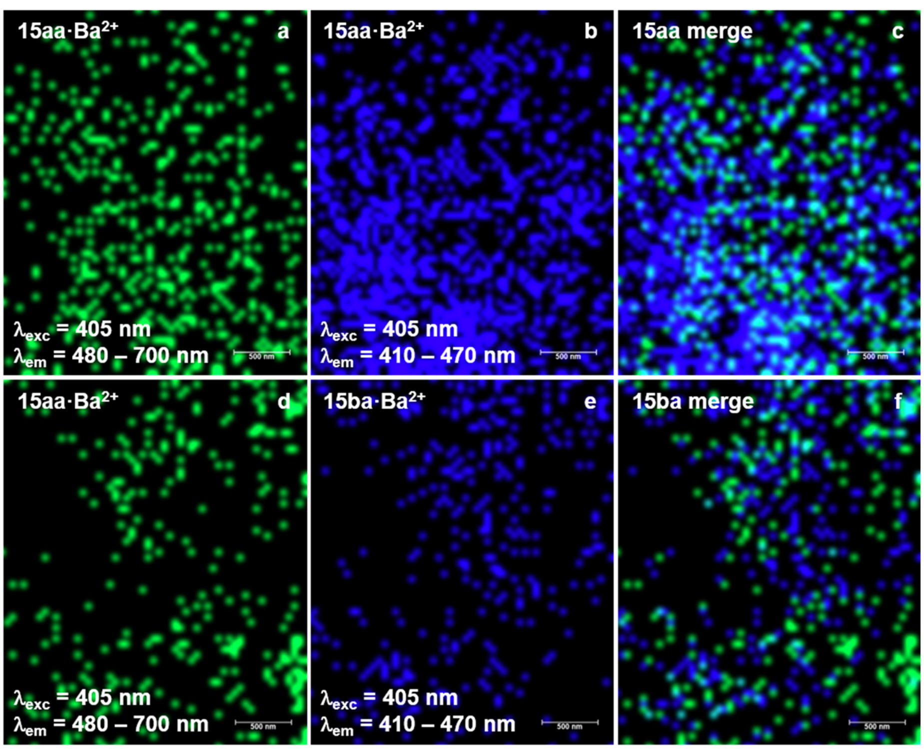

Fig. 12 Confocal microscopy images of compounds **15aa** (panels a–c) and **15ba** (panels d–f) on ITO after sublimation of barium triflate, at the unbound and Ba^{2+}-bound channels (see Fig. 11, panels c and f), promising candidates for barium tagging.

The same excitation pattern at 405 nm permitted the observation of blue signals in the 410–470 nm range, associated with the blue shift corresponding to barium tagging (Fig. 12, panels b and e). Since the images of samples containing **15aa** (panels a–c) and **15ba** (panels d–f) were recorded at the same area, merging both images permitted us to distinguish spots corresponding to the free and Ba^{2+} bound states for both FBI molecules, showing the excellent discrimination potential of our sensors. However, as the barium sublimation process cannot currently be performed *in situ*, it was not possible to capture images of the same zone before and after barium deposition. Therefore, as a control experiment, the samples shown in Fig. 12 were measured before sublimation of barium triflate in both wavelength ranges to ensure that no background signal at 410–470 nm could be misassigned to the sensor–Ba^{2+} complexes. Images of a different area of the sample of compound **15aa** deposited by means of spin coating over ITO without adding Ba^{2+} are gathered in the ESI† (Fig. S1).

Conclusion

In this paper, we report our results on the synthesis and evaluation of two families of fluorescent indicators for barium tagging. We have synthesised both families of sensors, including two types of crown ethers, two kinds of fluorophores, two spacers, and one silatrane group to facilitate anchoring these molecules to ITO surfaces. Our results show that the photophysical behavior of these compounds in solution does not vary significantly with respect to simpler non-functionalized analogues, thus confirming that, in general, incorporation of spacer–linker components does not affect the emission spectra of the fluorophores under analysis, thus making it feasible to analyse the photophysical properties of these molecules in solid–gas interfaces.[33] These results have been rationalized by TD-DFT calculations. Both FMI and FBI molecules show excellent binding properties, which make them very promising candidates for barium tagging. Monocolor indicators (FMIs) show a relative increase of the fluorescence intensity when barium is incorporated to these naphthyl fluorophores, thus dimming (but not vanishing) under these conditions the off–on character of this family of sensors on bare ITO surfaces. In the case of benzo[*a*]imidazo[5,1,2-*cd*]indolizine, the FBI behavior is preserved on going from solution to solid–gas interfaces. However, a partial quenching is observed with respect to the intensity observed in solution, as well as a significant decay in the molecular discrimination factors. These results suggest that the development of novel FMI and FBI molecules for barium tagging must take into account the partial quenching of the emission spectra on going from solution to functionalized surfaces, as well as a significant loss of discrimination factors and wider emission spectra. However, confocal microscopy experiments indicate that the bicolor character of FBI sensors is preserved. In summary, these combined solution–solid–gas interface studies suggest that future designs that incorporate FMIs and FBIs on tailor-made surfaces hold great promise for barium tagging in $\beta\beta0\nu$ experiments like NEXT.

Data availability

All experimental details including synthetic procedures, spectroscopic data, and theoretical calculation results are available in the ESI.†

Author contributions

Conception and design: D. N., F. W. F., B. J. P. J., J. J. G.-C., I. R. and F. P. C. Design of monocolor sensors: F. W. F. and B. J. P. J. Design of bicolour sensors: F. A.-L., I. R. and F. P. C. Chemical synthesis of sensors: F. A.-L., J. M.-C., I. V.-C., B. A., J. L. V. and I. R. Surface functionalization: F. A.-L., A. L., V. S., C. R. and I. R. AFM experiments: A. M., A. C. and C. M. Acquisition and analysis of data: F. A.-L., J. M.-C., I. V.-C., A. L., B. A., N. A., I. A., V. S., C. R., I. R., J. J. G.-C. and F. P. C. DFT calculations and analysis: I. V.-C., N. A. and F. P. C. Drafting the article, including ESI:† F. A.-L., I. R. and F. P. C. Revision and final edition of the manuscript: F. A.-L., F. W. F., B. J. P. J., J. J. G.-C., C. R., I. R. and F. P. C. Funding: J. J. G.-C. and F. P. C.

Conflicts of interest

There are no conflicts to declare.

Acknowledgements

Financial support for this work was provided by the European Research Council (ERC) under the European's Union Horizon 2020 research and innovation programme (H2020 ERC-SyG 951281), by the Spanish Ministerio de Ciencia, Innovación y Universidades (Grant PID2023-151549NB-I00, funded by MICIU/AEI/10.13039/501100011033 and by FEDER, EU) and by the Gobierno Vasco/Eusko Jaurlaritza (GV/EJ, Grant IT-1553-22). The authors thank the SGI/IZO-SGIker of the UPV/EHU and the DIPC for the generous allocation of analytical and computational resources. Technical assistance for confocal microscopy from Achucarro Basque Center for Neuroscience-Imaging Facility (UPV/EHU Scientific Park, Spain) is gratefully acknowledged.

Notes and references

1 M. Goeppert-Mayer, Double Beta-Disintegration, *Phys. Rev.*, 1935, **48**, 512–516.

2 G. Collaboration, M. Agostini, G. R. Araujo, A. M. Bakalyarov, M. Balata, I. Barabanov, L. Baudis, C. Bauer, E. Bellotti, S. Belogurov, A. Bettini, L. Bezrukov, V. Biancacci, D. Borowicz, E. Bossio, V. Bothe, V. Brudanin, R. Brugnera, A. Caldwell, C. Cattadori, A. Chernogorov, T. Comellato, V. D'Andrea, E. V. Demidova, N. Di Marco, E. Doroshkevich, F. Fischer, M. Fomina, A. Gangapshev, A. Garfagnini, C. Gooch, P. Grabmayr, V. Gurentsov, K. Gusev, J. Hakenmüller, S.

Hemmer, R. Hiller, W. Hofmann, J. Huang, M. Hult, L. V. Inzhechik, J. Janicskó Csáthy, J. Jochum, M. Junker, V. Kazalov, Y. Kermaïdic, H. Khushbakht, T. Kihm, I. V. Kirpichnikov, A. Klimenko, R. Kneißl, K. T. Knöpfle, O. Kochetov, V. N. Kornoukhov, P. Krause, V. V. Kuzminov, M. Laubenstein, A. Lazzaro, M. Lindner, I. Lippi, A. Lubashevskiy, B. Lubsandorzhiev, G. Lutter, C. Macolino, B. Majorovits, W. Maneschg, L. Manzanillas, M. Miloradovic, R. Mingazheva, M. Misiaszek, P. Moseev, Y. Müller, I. Nemchenok, K. Panas, L. Pandola, K. Pelczar, L. Pertoldi, P. Piseri, A. Pullia, C. Ransom, L. Rauscher, S. Riboldi, N. Rumyantseva, C. Sada, F. Salamida, S. Schönert, J. Schreiner, M. Schütt, A. K. Schütz, O. Schulz, M. Schwarz, B. Schwingenheuer, O. Selivanenko, E. Shevchik, M. Shirchenko, L. Shtembari, H. Simgen, A. Smolnikov, D. Stukov, A. A. Vasenko, A. Veresnikova, C. Vignoli, K. von Sturm, T. Wester, C. Wiesinger, M. Wojcik, E. Yanovich, B. Zatschler, I. Zhitnikov, S. V. Zhukov, D. Zinatulina, A. Zschocke, A. J. Zsigmond, K. Zuber and G. Zuzel, Final Results of GERDA on the Search for Neutrinoless Double-β Decay, *Phys. Rev. Lett.*, 2020, **125**, 252502.

3 L.-Z. C. Kam, S. Abe, S. Asami, M. Eizuka, S. Futagi, A. Gando, Y. Gando, T. Gima, A. Goto, T. Hachiya, K. Hata, S. Hayashida, K. Hosokawa, K. Ichimura, S. Ieki, H. Ikeda, K. Inoue, K. Ishidoshiro, Y. Kamei, N. Kawada, Y. Kishimoto, M. Koga, M. Kurasawa, N. Maemura, T. Mitsui, H. Miyake, T. Nakahata, K. Nakamura, K. Nakamura, R. Nakamura, H. Ozaki, T. Sakai, H. Sambonsugi, I. Shimizu, J. Shirai, K. Shiraishi, A. Suzuki, Y. Suzuki, A. Takeuchi, K. Tamae, K. Ueshima, H. Watanabe, Y. Yoshida, S. Obara, A. K. Ichikawa, D. Chernyak, A. Kozlov, K. Z. Nakamura, S. Yoshida, Y. Takemoto, S. Umehara, K. Fushimi, K. Kotera, Y. Urano, B. E. Berger, B. K. Fujikawa, J. G. Learned, J. Maricic, S. N. Axani, J. Smolsky, Z. Fu, L. A. Winslow, Y. Efremenko, H. J. Karwowski, D. M. Markoff, W. Tornow, S. Dell'Oro, T. O'Donnell, J. A. Detwiler, S. Enomoto, M. P. Decowski, C. Grant, A. Li and H. Song, Search for the Majorana Nature of Neutrinos in the Inverted Mass Ordering Region with KamLAND-Zen, *Phys. Rev. Lett.*, 2023, **130**, 051801.

4 N. Aghanim, Y. Akrami, M. Ashdown, J. Aumont, C. Baccigalupi, M. Ballardini, A. J. Banday, R. B. Barreiro, N. Bartolo, S. Basak, R. Battye, K. Benabed, J. P. Bernard, M. Bersanelli, P. Bielewicz, J. J. Bock, J. R. Bond, J. Borrill, F. R. Bouchet, F. Boulanger, M. Bucher, C. Burigana, R. C. Butler, E. Calabrese, J. F. Cardoso, J. Carron, A. Challinor, H. C. Chiang, J. Chluba, L. P. L. Colombo, C. Combet, D. Contreras, B. P. Crill, F. Cuttaia, P. de Bernardis, G. de Zotti, J. Delabrouille, J. M. Delouis, E. Di Valentino, J. M. Diego, O. Doré, M. Douspis, A. Ducout, X. Dupac, S. Dusini, G. Efstathiou, F. Elsner, T. A. Enßlin, H. K. Eriksen, Y. Fantaye, M. Farhang, J. Fergusson, R. Fernandez-Cobos, F. Finelli, F. Forastieri, M. Frailis, A. A. Fraisse, E. Franceschi, A. Frolov, S. Galeotta, S. Galli, K. Ganga, R. T. Génova-Santos, M. Gerbino, T. Ghosh, J. González-Nuevo, K. M. Górski, S. Gratton, A. Gruppuso, J. E. Gudmundsson, J. Hamann, W. Handley, F. K. Hansen, D. Herranz, S. R. Hildebrandt, E. Hivon, Z. Huang, A. H. Jaffe, W. C. Jones, A. Karakci, E. Keihänen, R. Keskitalo, K. Kiiveri, J. Kim, T. S. Kisner, L. Knox, N. Krachmalnicoff, M. Kunz, H. Kurki-Suonio, G. Lagache, J. M. Lamarre, A. Lasenby, M. Lattanzi, C. R. Lawrence, M. Le Jeune, P. Lemos, J. Lesgourgues, F. Levrier, A. Lewis, M. Liguori, P. B. Lilje, M. Lilley, V. Lindholm, M. López-Caniego, P. M. Lubin, Y. Z. Ma, J. F. Macías-Pérez, G. Maggio, D. Maino, N. Mandolesi, A. Mangilli, A. Marcos-Caballero, M. Maris, P. G. Martin, M. Martinelli, E. Martínez-González, S. Matarrese, N. Mauri, J. D. McEwen, P. R. Meinhold, A. Melchiorri, A. Mennella, M. Migliaccio, M. Millea, S. Mitra, M. A. Miville-Deschênes, D. Molinari, L. Montier, G. Morgante, A. Moss, P. Natoli, H. U. Nørgaard-Nielsen, L. Pagano, D. Paoletti, B. Partridge, G. Patanchon, H. V. Peiris, F. Perrotta, V. Pettorino, F. Piacentini, L. Polastri, G. Polenta, J. L. Puget, J. P. Rachen, M. Reinecke, M. Remazeilles, A. Renzi, G. Rocha, C. Rosset, G. Roudier, J. A. Rubiño-Martín, B. Ruiz-Granados, L. Salvati, M. Sandri, M. Savelainen, D. Scott, E. P. S. Shellard, C. Sirignano, G. Sirri, L. D. Spencer, R. Sunyaev, A. S. Suur-Uski, J. A. Tauber, D. Tavagnacco, M. Tenti, L. Toffolatti, M. Tomasi, T. Trombetti, L. Valenziano, J. Valiviita, B. Van Tent, L. Vibert, P. Vielva, F. Villa, N. Vittorio, B. D. Wandelt, I. K. Wehus, M. White, S. D. M. White, A. Zacchei and A. Zonca, Planck 2018 results. VI. Cosmological parameters, *Astron. Astrophys.*, 2020, **641**(A6), 1–67.

5 E. Majorana, Teoria simmetrica dell'elettrone e del positrone, *Nuovo Cimento*, 1937, **14**, 171–184.

6 D. S. Andrei, Violation of CP invariance, C asymmetry, and baryon asymmetry of the universe, *Soviet*, *Phys.-Usp.*, 1991, **34**, 392.

7 M. Fukugita and T. Yanagida, Barygenesis without grand unification, *Phys. Lett. B*, 1986, **174**, 45–47.

8 M. K. Moe, Detection of neutrinoless double-beta decay, *Phys. Rev. C: Nucl. Phys.*, 1991, **44**, R931–R934.

9 D. R. Nygren, Detecting the barium daughter in 136Xe 0-$\nu\beta\beta$ decay using single-molecule fluorescence imaging techniques, *J. Phys.: Conf. Ser.*, 2015, **650**, 012002.

10 C. Chambers, T. Walton, D. Fairbank, A. Craycraft, D. R. Yahne, J. Todd, A. Iverson, W. Fairbank, A. Alamre, J. B. Albert, G. Anton, I. J. Arnquist, I. Badhrees, P. S. Barbeau, D. Beck, V. Belov, T. Bhatta, F. Bourque, J. P. Brodsky, E. Brown, T. Brunner, A. Burenkov, G. F. Cao, L. Cao, W. R. Cen, S. A. Charlebois, M. Chiu, B. Cleveland, M. Coon, M. Côté, W. Cree, J. Dalmasson, T. Daniels, L. Darroch, S. J. Daugherty, J. Daughhetee, S. Delaquis, A. Der Mesrobian-Kabakian, R. DeVoe, J. Dilling, Y. Y. Ding, M. J. Dolinski, A. Dragone, J. Echevers, L. Fabris, J. Farine, S. Feyzbakhsh, R. Fontaine, D. Fudenberg, G. Gallina, G. Giacomini, R. Gornea, G. Gratta, E. V. Hansen, M. Heffner, E. W. Hoppe, J. Hößl, A. House, P. Hufschmidt, M. Hughes, Y. Ito, A. Jamil, C. Jessiman, M. J. Jewell, X. S. Jiang, A. Karelin, L. J. Kaufman, D. Kodroff, T. Koffas, S. Kravitz, R. Krücken, A. Kuchenkov, K. S. Kumar, Y. Lan, A. Larson, D. S. Leonard, G. Li, S. Li, Z. Li, C. Licciardi, Y. H. Lin, P. Lv, R. MacLellan, T. Michel, B. Mong, D. C.

Moore, K. Murray, R. J. Newby, Z. Ning, O. Njoya, F. Nolet, O. Nusair, K. Odgers, A. Odian, M. Oriunno, J. L. Orrell, G. S. Ortega, I. Ostrovskiy, C. T. Overman, S. Parent, A. Piepke, A. Pocar, J. F. Pratte, D. Qiu, V. Radeka, E. Raguzin, T. Rao, S. Rescia, F. Retière, A. Robinson, T. Rossignol, P. C. Rowson, N. Roy, R. Saldanha, S. Sangiorgio, S. Schmidt, J. Schneider, A. Schubert, K. Skarpaas, A. K. Soma, G. St-Hilaire, V. Stekhanov, T. Stiegler, X. L. Sun, M. Tarka, T. Tolba, T. I. Totev, R. Tsang, T. Tsang, F. Vachon, B. Veenstra, V. Veeraraghavan, G. Visser, J. L. Vuilleumier, M. Wagenpfeil, Q. Wang, J. Watkins, M. Weber, W. Wei, L. J. Wen, U. Wichoski, G. Wrede, S. X. Wu, W. H. Wu, Q. Xia, L. Yang, Y. R. Yen, O. Zeldovich, X. Zhang, J. Zhao, Y. Zhou and T. Ziegler, Imaging individual barium atoms in solid xenon for barium tagging in nEXO, *Nature*, 2019, **569**, 203–207.

11 N. Collaboration, A. D. McDonald, B. J. P. Jones, D. R. Nygren, C. Adams, V. Álvarez, C. D. R. Azevedo, J. M. Benlloch-Rodríguez, F. I. G. M. Borges, A. Botas, S. Cárcel, J. V. Carrión, S. Cebrián, C. A. N. Conde, J. Díaz, M. Diesburg, J. Escada, R. Esteve, R. Felkai, L. M. P. Fernandes, P. Ferrario, A. L. Ferreira, E. D. C. Freitas, A. Goldschmidt, J. J. Gómez-Cadenas, D. González-Díaz, R. M. Gutiérrez, R. Guenette, K. Hafidi, J. Hauptman, C. A. O. Henriques, A. I. Hernandez, J. A. Hernando Morata, V. Herrero, S. Johnston, L. Labarga, A. Laing, P. Lebrun, I. Liubarsky, N. López-March, M. Losada, J. Martín-Albo, G. Martínez-Lema, A. Martínez, F. Monrabal, C. M. B. Monteiro, F. J. Mora, L. M. Moutinho, J. Muñoz Vidal, M. Musti, M. Nebot-Guinot, P. Novella, B. Palmeiro, A. Para, J. Pérez, M. Querol, J. Repond, J. Renner, S. Riordan, L. Ripoll, J. Rodríguez, L. Rogers, F. P. Santos, J. M. F. dos Santos, A. Simón, C. Sofka, M. Sorel, T. Stiegler, J. F. Toledo, J. Torrent, Z. Tsamalaidze, J. F. C. A. Veloso, R. Webb, J. T. White and N. Yahlali, Demonstration of Single-Barium-Ion Sensitivity for Neutrinoless Double-Beta Decay Using Single-Molecule Fluorescence Imaging, *Phys. Rev. Lett.*, 2018, **120**, 132504.

12 N. Collaboration, P. Novella, M. Sorel, A. Usón, C. Adams, H. Almazán, V. Álvarez, B. Aparicio, A. I. Aranburu, L. Arazi, I. J. Arnquist, S. Ayet, C. D. R. Azevedo, K. Bailey, F. Ballester, J. M. Benlloch-Rodríguez, F. I. G. M. Borges, S. Bounasser, N. Byrnes, S. Cárcel, J. V. Carrión, S. Cebrián, E. Church, C. A. N. Conde, T. Contreras, F. P. Cossío, A. A. Denisenko, G. Díaz, J. Díaz, T. Dickel, J. Escada, R. Esteve, A. Fahs, R. Felkai, L. M. P. Fernandes, P. Ferrario, A. L. Ferreira, F. W. Foss, E. D. C. Freitas, Z. Freixa, J. Generowicz, A. Goldschmidt, J. J. Gómez-Cadenas, R. González, D. González-Díaz, R. Guenette, R. M. Gutiérrez, J. Haefner, K. Hafidi, J. Hauptman, C. A. O. Henriques, J. A. Hernando Morata, P. Herrero-Gómez, V. Herrero, J. Ho, Y. Ifergan, B. J. P. Jones, M. Kekic, L. Labarga, A. Laing, L. Larizgoitia, P. Lebrun, D. Lopez Gutierrez, N. López-March, M. Losada, R. D. P. Mano, J. Martín-Albo, A. Martínez, G. Martínez-Lema, M. Martínez-Vara, A. D. McDonald, Z. E. Meziani, K. Mistry, F. Monrabal, C. M. B. Monteiro, F. J. Mora, J. Muñoz Vidal, K. Navarro, D. R. Nygren, E. Oblak, M. Odriozola-Gimeno, B. Palmeiro, A. Para, J. Pérez, M. Querol, A. Raymond, A. B. Redwine, J. Renner, L. Ripoll, I. Rivilla, Y. Rodríguez García, J. Rodríguez, C. Rogero, L. Rogers, B. Romeo, C. Romo-Luque, F. P. Santos, J. M. F. dos Santos, A. Simón, C. Stanford, J. M. R. Teixeira, P. Thapa, J. F. Toledo, J. Torrent, J. F. C. A. Veloso, T. T. Vuong, R. Webb, J. T. White, K. Woodruff and N. Yahlali, Measurement of the ^{136}Xe two-neutrino double-β-decay half-life via direct background subtraction in NEXT, *Phys. Rev. C*, 2022, **105**, 055501.

13 Z. Freixa, I. Rivilla, F. Monrabal, J. J. Gómez-Cadenas and F. P. Cossío, Bibehaviour fluorescent molecular sensors for cations: design and experimental validation, *Phys. Chem. Chem. Phys.*, 2021, **23**, 15440–15457.

14 V. F. Sidorkin, E. F. Belogolova, E. P. Doronina, G. Liu, S. M. Ciborowski and K. H. Bowen, "Outlaw" Dipole-Bound centrecentrecentreAnions of Intra-Molecular Complexes, *J. Am. Chem. Soc.*, 2020, **142**, 2001–2011.

15 K. L. Materna, B. J. Brennan and G. W. Brudvig, Silatranes for binding inorganic complexes to metal oxide surfaces, *Dalton Trans.*, 2015, **44**, 20312–20315.

16 S. Fery-Forgues, M. T. Le Bris, J. P. Guette and B. Valeur, Ion-responsive fluorescent compounds. 1. Effect of cation binding on photophysical properties of benzoxazinone derivative linked to monoaza-15-crown-5, *J. Phys. Chem.*, 1988, **92**, 6233–6237.

17 J. Li, D. Yim, W.-D. Jang and J. Yoon, Recent progress in the design and applications of fluorescence probes containing crown ethers, *Chem. Soc. Rev.*, 2017, **46**, 2437–2458.

18 B. Daly, J. Ling and A. P. de Silva, Current developments in fluorescent PET (photoinduced electron transfer) sensors and switches, *Chem. Soc. Rev.*, 2015, **44**, 4203–4211.

19 P. Thapa, I. Arnquist, N. Byrnes, A. A. Denisenko, F. W. Foss, B. J. P. Jones, A. D. McDonald, D. R. Nygren and K. Woodruff, Barium Chemosensors with Dry-Phase Fluorescence for Neutrinoless Double Beta Decay, *Sci. Rep.*, 2019, **9**, 15097.

20 P. Thapa, N. K. Byrnes, A. A. Denisenko, J. X. Mao, A. D. McDonald, C. A. Newhouse, T. T. Vuong, K. Woodruff, K. Nam, D. R. Nygren, B. J. P. Jones and F. W. Foss, Jr., Demonstration of Selective Single-Barium Ion Detection with Dry Diazacrown Ether Naphthalimide Turn-on Chemosensors, *ACS Sens.*, 2021, **6**, 192–202.

21 M. Aginagalde, Y. Vara, A. Arrieta, R. Zangi, V. L. Cebolla, A. Delgado-Camón and F. P. Cossío, Tandem [8 + 2] Cycloaddition−[2 + 6 + 2] Dehydrogenation Reactions Involving Imidazo[1,2-a]pyridines and Imidazo[1,2-a]pyrimidines, *J. Org. Chem.*, 2010, **75**, 2776–2784.

22 P. Herrero-Gómez, J. P. Calupitan, M. Ilyn, A. Berdonces-Layunta, T. Wang, D. G. de Oteyza, M. Corso, R. González-Moreno, I. Rivilla, B. Aparicio, A. I. Aranburu, Z. Freixa, F. Monrabal, F. P. Cossío, J. J. Gómez-Cadenas, C. Rogero, C. Adams, H. Almazán, V. Álvarez, L. Arazi, I. J. Arnquist, S. Ayet, C. D. R. Azevedo, K. Bailey, F. Ballester, J. M. Benlloch-Rodríguez, F. I. G. M. Borges, S. Bounasser, N. Byrnes, S. Cárcel, J. V. Carrión, S. Cebrián, E. Church, C. A. N. Conde, T. Contreras, A. A. Denisenko, E. Dey, G. Díaz, T. Dickel, J. Escada, R. Esteve, A. Fahs, R. Felkai, L. M. P. Fernandes, P. Ferrario, A. L. Ferreira, F. W. Foss, E. D. C. Freitas, Z. Freixa,

J. Generowicz, A. Goldschmidt, R. González-Moreno, R. Guenette, J. Haefner, K. Hafidi, J. Hauptman, C. A. O. Henriques, J. A. H. Morata, V. Herrero, J. Ho, P. Ho, Y. Ifergan, B. J. P. Jones, M. Kekic, L. Labarga, L. Larizgoitia, P. Lebrun, D. L. Gutierrez, N. López-March, R. Madigan, R. D. P. Mano, J. Martín-Albo, G. Martínez-Lema, M. Martínez-Vara, Z. E. Meziani, R. Miller, K. Mistry, C. M. B. Monteiro, F. J. Mora, J. M. Vidal, K. Navarro, P. Novella, A. Nuñez, D. R. Nygren, E. Oblak, M. Odriozola-Gimeno, B. Palmeiro, A. Para, M. Querol, A. B. Redwine, J. Renner, L. Ripoll, J. Rodríguez, L. Rogers, B. Romeo, C. Romo-Luque, F. P. Santos, J. M. F. dos Santos, A. Simón, M. Sorel, C. Stanford, J. M. R. Teixeira, J. F. Toledo, J. Torrent, A. Usón, J. F. C. A. Veloso, T. T. Vuong, J. Waiton, J. T. White and N. Collaboration, Ba+2 ion trapping using organic submonolayer for ultra-low background neutrinoless double beta detector, *Nat. Commun.*, 2022, **13**, 7741.

23 I. Rivilla, B. Aparicio, J. M. Bueno, D. Casanova, C. Tonnelé, Z. Freixa, P. Herrero, C. Rogero, J. I. Miranda, R. M. Martínez-Ojeda, F. Monrabal, B. Olave, T. Schäfer, P. Artal, D. Nygren, F. P. Cossío and J. J. Gómez-Cadenas, Fluorescent bicolour sensor for low-background neutrinoless double β decay experiments, *Nature*, 2020, **583**, 48–54.

24 J. W. Sibert, P. B. Forshee, G. R. Hundt, A. L. Sargent, S. G. Bott and V. Lynch, Wurster's Crowns: A Comparative Study of ortho- and para-Phenylenediamine-Containing Macrocyclic Receptors, *Inorg. Chem.*, 2007, **46**, 10913–10925.

25 P. Deveci, B. Taner, Z. Üstündağ, E. Özcan, A. O. Solak and Z. Kılıç, Synthesis, enhanced spectroscopic characterization and electrochemical grafting of N-(4-aminophenyl)aza-18-crown-6: Application of DEPT, HETCOR, HMBC-NMR and X-ray photoelectron spectroscopy, *J. Mol. Struct.*, 2010, **982**, 162–168.

26 R. W. Sabnis, Novel Peptidylarginine Deiminase Type 4 (PAD4) Inhibitors, *ACS Med. Chem. Lett.*, 2022, **13**, 1537–1538.

27 R. Semwal, A. Joshi, R. Kumar and S. Adimurthy, Annulation of imidazo[1,2-a]pyridines under metal-free conditions, *New J. Chem.*, 2020, **44**, 20530–20534.

28 A. Suzuki, Cross-Coupling Reactions Of Organoboranes: An Easy Way To Construct C–C Bonds (Nobel Lecture), *Angew. Chem., Int. Ed.*, 2011, **50**, 6722–6737.

29 N. Miyaura and A. Suzuki, Palladium-Catalyzed Cross-Coupling Reactions of Organoboron Compounds, *Chem. Rev.*, 1995, **95**, 2457–2483.

30 C. T. Pan, T. T. Wu, J. K. Tseng, C. Y. Su, W. J. Wang and J. C. Huang, Mechanical behavior of metallic glasses Mg–Cu–Y using nano-indentation, *Microsyst. Technol.*, 2010, **16**, 585–593.

31 A. A. Tseng, J.-I. Shirakashi, S. Nishimura, K. Miyashita and A. Notargiacomo, Scratching properties of nickel-iron thin film and silicon using atomic force microscopy, *J. Appl. Phys.*, 2009, **106**, 044314.

32 Y. Yan, S. Chang, T. Wang and Y. Geng, Scratch on Polymer Materials Using AFM Tip-Based Approach: A Review, *Polymer*, 2019, **11**, 1590.

33 N. K. Byrnes, A. A. Denisenko, F. W. Foss, B. J. P. Jones, A. D. McDonald, D. R. Nygren, P. Thapa and K. Woodruff, Barium Tagging with Selective, Dry-Functional, Single Molecule Sensitive On-Off Fluorophores for the NEXT Experiment, *arXiv*, 2019, preprint, DOI: **10.48550/arXiv.1909.04677**.

34 K. P. Carter, A. M. Young and A. E. Palmer, Fluorescent Sensors for Measuring Metal Ions in Living Systems, *Chem. Rev.*, 2014, **114**, 4564–4601.

35 A. Wolfe, G. H. Shimer, Jr. and T. Meehan, Polycyclic aromatic hydrocarbons physically intercalate into duplex regions of denatured DNA, *Biochemistry*, 1987, **26**, 6392–6396.

36 A. D. Ardianrama, A. Pradyasti, H.-C. Woo and M. H. Kim, Colorimetric sensing of barium ion in water based on polyelectrolyte-induced chemical etching of silver nanoprisms, *Dyes Pigm.*, 2020, **181**, 108578.

37 A. K. K. Bhasin, P. Chauhan and S. Chaudhary, A novel sulfur-incorporated naphthoquinone as a selective “turn-on” fluorescence chemical sensor for rapid detection of Ba2+ ion in semi-aqueous medium, *Sens. Actuators, B*, 2019, **294**, 116–122.

38 P. Ravichandiran, S. A. Subramaniyan, A. P. Bella, P. M. Johnson, A. R. Kim, K. S. Shim and D. J. Yoo, Simple Fluorescence Turn-On Chemosensor for Selective Detection of Ba2+ Ion and Its Live Cell Imaging, *Anal. Chem.*, 2019, **91**, 10095–10101.

39 D. Yun, E. Cho, S. D. Dindulkar and S. Jung, Succinoglycan Octasaccharide Conjugated Polydiacetylene-Doped Alginate Beads for Barium (II) Detection, *Macromol. Mater. Eng.*, 2016, **301**, 805–811.

40 L. Zhao, D. Sui and Y. Wang, Luminescent properties of N-salicylidene-3-aminopyridine and selective sensing behavior to Ba2+, *J. Lumin.*, 2015, **162**, 81–86.

41 R. Bauernschmitt and R. Ahlrichs, Treatment of electronic excitations within the adiabatic approximation of time dependent density functional theory, *Chem. Phys. Lett.*, 1996, **256**, 454–464.

42 M. J. Frisch, G. W. Trucks and H. B. Schlegel *et al.*, *Gaussian 16, Revision C.01*, Gaussian, Inc., Wallingford, CT, 2016.

43 F. Weigend and R. Ahlrichs, Balanced basis sets of split valence, triple zeta valence and quadruple zeta valence quality for H to Rn: Design and assessment of accuracy, *Phys. Chem. Chem. Phys.*, 2005, **7**, 3297–3305.

44 Y. Zhao and D. G. Truhlar, Density Functionals with Broad Applicability in Chemistry, *Acc. Chem. Res.*, 2008, **41**, 157–167.

45 P. R. Nicovich, X. Lu, K. Gaus and J. J. Gooding, Characterization of functionalized glass and indium tin oxide surfaces as substrates for super-resolution microscopy, *J. Phys. D: Appl. Phys.*, 2019, **52**, 034003.